TITANIUM-BASED METAL-ORGANIC FRAMEWORK AND ITS MODIFICATIONS BY THERMAL DECOMPOSITION FOR VISIBLE LIGHT PHOTOCATALYTIC ACTIVITY

NUR SHAZWANI BINTI ABDUL MUBARAK

UNIVERSITI SAINS MALAYSIA

2024

TITANIUM-BASED METAL-ORGANIC FRAMEWORK AND ITS MODIFICATIONS BY THERMAL DECOMPOSITION FOR VISIBLE LIGHT PHOTOCATALYTIC ACTIVITY

by

NUR SHAZWANI BINTI ABDUL MUBARAK

Thesis submitted in fulfilment of the requirements for the degree of Doctor of Philosophy

March 2024

ACKNOWLEDGEMENT

First and foremost, I would like to express my deep gratitude to my supervisor, Dr. Sumiyyah Sabar, for her guidance and support throughout my PhD journey. I am also immensely grateful to my co-supervisors, Professor Raphaël Schneider, and Associate Professor Dr. Foo Yuen Keng, for their invaluable contributions, and insightful feedback.

In addition, I would like to extend my heartfelt appreciation to my best friend, Saifulddin, whose support, encouragement, and knowledge sharing have been instrumental in my academic pursuits. His friendship has been a constant source of motivation and inspiration. I am also deeply thankful to my circle of friends at USM, including Norma, Najwa, Hidayah, Choong, Esan, Anis, Fatin, Nana, Izzati, and Yusra for their support throughout my studies. Their friendship has made this journey more enjoyable and fulfilling.

Furthermore, I would like to express my gratitude to the entire team of officers, lab assistants, and lecturers at USM, particularly in the School of Chemical Sciences, School of Physics, School of Technology Industry, School of Materials and Mineral Resources Engineering, Center for Global Archaeological Research, and Advanced Medical and Dental Institute (IPPT). Their selfless assistance and unconditional help have been beneficial in the success of my research. I would also like to acknowledge the generous support of Universiti Sains Malaysia (USM) for granting me the scholarship under the USM Fellowship program. The financial support from the Ministry of Higher Education (MOHE), Malaysia, through the Hubert Curien Partnership-Hibiscus (PHC-Hibiscus) Grant (203/PJJAUH/6782001), is sincerely appreciated.

Finally, I would like to dedicate this achievement to my late father, Abdul Mubarak, and beloved mother, Azezah Ibrahim, as well as my five sisters, Azhana, Shahrizat, Elani, Nisha, and Sheham. Their unconditional support, both financially and emotionally, has been the cornerstone of my success throughout my PhD journey. I am eternally grateful for their love, sacrifices, and firm belief in me. This thesis is dedicated from the depths of my heart to my mother, who has been my pillar of strength, constantly providing guidance and prayers throughout my research. Finally, I would like to express my heartfelt appreciation to my mischievous cat, Rio, for being a constant source of companionship and comfort during the ups and downs of this journey.

TABLE OF CONTENTS

ACK	NOWLEI	OGEMENT	ii
TABI	LE OF CO	ONTENTS	iv
LIST	OF TAB	LES	X
LIST	OF FIGU	JRES	xii
LIST	OF SYM	BOLS	xix
LIST	OF ABB	REVIATIONS	XX
LIST	OF APPI	ENDICES	xxii
ABST	Γ RAK		xxiii
ABST	TRACT		xxvi
СНА	PTER 1	INTRODUCTION	1
1.1	Research	n Background	1
1.2	Problem	Statements	7
1.3	Research	n Objectives	8
1.4	Scope of	Research	9
СНА	PTER 2	LITERATURE REVIEW	11
2.1	Wastewa	ater Treatment Method	11
2.2	Advance	ed Oxidation Process (AOP)	13
2.3	Photocat	alysis	14
	2.3.1	Titanium Dioxide (TiO ₂)	15
	2.3.2	TiO ₂ as Photocatalyst	18
	2.3.3	Carbon Porous TiO ₂	20
2.4	Metal-O	rganic Frameworks	21
2.5	Ti-based	MOF	23
2.6	MIL-125	5(Ti)	24
2.7	Modifica	ation of MIL-125(Ti)	26

	2.7.1	Ligand functionalization
	2.7.2	Doping
	2.7.3	Heterostructures
2.8	Thermal	Decomposition of MIL-125(Ti) and MIL-125-NH ₂
2.9	Dyes as	Organic Pollutants
	2.9.1	Methylene Blue (MB)
2.10	Summar	y53
CHA	PTER 3	MATERIALS AND METHOD55
3.1	Chemica	als and Materials
3.2	Analytic	al Techniques
3.3	•	s of Nitrogen-doped Carbon Porous (NCP) TiO ₂ Derived MIL-125-
	3.3.1	Preparation of MIL-125-NH ₂
	3.3.2	Preparation of NCP TiO ₂ Derived MIL-125-NH ₂
3.4	Synthesi	s of NCP Nickel-doped TiO ₂ Derived MIL-125-NH ₂
	3.4.1	Preparation of Ni ²⁺ Ion Precursor
	3.4.2	Preparation of Ni-doped MIL-125-NH ₂
	3.4.3	Preparation of NCP Ni-doped TiO ₂ Derived MIL-125-NH ₂ 59
3.5	Synthesi	s of composite NCP ZnO/TiO ₂ Derived MIL-125-NH ₂
	3.5.1	Preparation of Zn-MIL-125-NH ₂
	3.5.2	Preparation of Composite NCP ZnO/TiO ₂ Derived MIL-125-NH ₂
3.6	Characte	erization of Photocatalysts
	3.6.1	X-ray Powder Diffraction (PXRD)
	3.6.2	Fourier Transform Infrared Spectroscopy (FTIR)
	3.6.3	Scanning Electron Microscopy/Energy Dispersive X-ray (SEM-EDX)
	3.6.4	N ₂ Adsorption-desorption (BET) Analysis

	3.6.5	Thermogravimetric Analysis (TGA)	62
	3.6.6	Raman spectroscopy	62
	3.6.7	Ultraviolet-visible Diffuse Reflectance Spectroscopy (UV-DRS)	63
	3.6.8	Photoluminescence Spectroscopy (PL)	63
	3.6.9	X-ray Photoelectron Spectroscopy (XPS)	63
	3.6.10	Determination of Point of Zero Charge (pH _{pzc})	64
3.7	Preparati	ion of MB solution	64
3.8	Photocat	alytic Activity	65
	3.8.1	Effect of Photocatalyst Loading	66
	3.8.2	Effect of Initial Solution pH	66
	3.8.3	Effect of Initial MB Concentration	67
3.9	Reusabil	ity Study	67
3.10	Minerali	zation Studies	67
3.11	Mechani	stic Study	68
3.12	Detection	n of Intermediates	68
3.13	Photocat	alytic Performance of Other Organic Pollutants	69
СНА	PTER 4	RESULTS AND DISCUSSION NCP TiO ₂ DERIVED MIL-125-NH ₂	71
4.1	Introduc	tion	71
4.2		ntion of synthesis parameters for Nitrogen-carbon Porous (NCP)	72
	4.2.1	Effect of Atmospheric Condition	72
	4.2.2	Effect of Calcination Temperature on MIL-125-NH ₂	77
4.3	Characte	rization of NCP TiO ₂	79
	4.3.1	X-ray Powder Diffraction Spectroscopy (PXRD)	79
	4.3.2	Fourier Transform Infrared Spectroscopy (FTIR)	82
	4.3.3	Scanning Electron Microscopy-Energy Dispersive X-ray (SEM-EDX)	84

	4.3.4	N ₂ Adsorption-desorption (BET) Analysis	88
	4.3.5	Thermogravimetric Analysis (TGA)	90
	4.3.6	Raman Spectroscopy	91
	4.3.7	Ultraviolet-visible Diffuse Reflectance Spectroscopy (UV-DRS)	93
	4.3.8	Photoluminescence Spectroscopy (PL)	95
	4.3.9	X-ray Photoelectron Spectroscopy (XPS)	97
4.4	Photoca	talytic Activity of NCP TiO ₂	100
	4.4.1	Photocatalytic Performance Evaluation	100
	4.4.2	Kinetic Study	103
	4.4.3	Reusability Study	104
	4.4.4	Mineralization Studies	106
	4.4.5	Mechanistic Study	107
	4.4.6	Photodegradation of Other Organic Pollutants	111
4.5	Compar	ison study with other materials	113
4.6	Summar	-y	114
СНА	PTER 5	RESULTS AND DISCUSSION NCP Ni-DOPED TiO ₂ DERIVED MIL-125-NH ₂	115
5.1	Introduc	etion	115
5.2	Optimiz	ation of synthesis parameters for NCP Ni-doped TiO ₂	116
	5.2.1	Effect of Weight Percent Ni Dopant	116
	5.2.2	Effect of Calcination Temperature	118
5.3	Characte	erization of NCP Ni-doped TiO ₂	120
	5.3.1	X-ray Powder Diffraction Spectroscopy (PXRD)	120
	5.3.2	Fourier Transform Infrared Spectroscopy (FTIR)	123
	5.3.3	Scanning Electron Microscopy-Energy Dispersive X-ray (SEM-EDX)	125
	5.3.4	N ₂ Adsorption-desorption (BET) Analysis	128

	5.3.5	Thermogravimetric Analysis (TGA)
	5.3.6	Raman Spectroscopy
	5.3.7	Ultraviolet-visible Diffuse Reflectance Spectroscopy (UV-DRS)
	5.3.8	Photoluminescence Spectroscopy (PL)
	5.3.9	X-ray Photoelectron Spectroscopy (XPS)
5.4	Photoca	talytic activity of NCP Ni-Doped TiO ₂ 140
	5.4.1	Photocatalytic Performance Evaluation
	5.4.2	Kinetic Study
	5.4.3	Reusability Study
	5.4.4	Mineralization Studies
	5.4.5	Mechanistic Study
	5.4.6	Photocatalytic Performance of Other Organic Pollutants
5.5	Compar	ison study with other materials
5.6	Summar	y
СНА	PTER 6	RESULTS AND DISCUSSION NCP ZnO/TiO ₂ DERIVED MIL-125-NH ₂
6.1	Introduc	tion
6.2	Optimiz	ation of synthesis parameters for NCP ZnO/TiO ₂
	6.2.1	Effect of Zn on MIL-125-NH ₂
	6.2.2	Effect of calcination temperature
6.3	Characte	erization of NCP ZnO/TiO ₂ 161
	6.3.1	X-ray Powder Diffraction Spectroscopy (PXRD)161
	6.3.2	Fourier Transform Infrared Spectroscopy (FTIR) 163
	6.3.3	Scanning Electron Microscopy-Energy Dispersive X-ray (SEM-EDX)
	6.3.4	N ₂ Adsorption-desorption (BET) Analysis
	6.3.5	Thermogravimetric Analysis (TGA)

	6.3.6	Raman Spectroscopy	. 172
	6.3.7	Ultraviolet-visible Diffuse Reflectance Spectroscopy (UV-DRS)	. 174
	6.3.8	Photoluminescence Spectroscopy (PL)	. 177
	6.3.9	X-ray Photoelectron Spectroscopy (XPS)	. 178
6.4	Photocata	alytic activity of NCP ZnO/TiO2	. 181
	6.4.1	Photocatalytic Performance Evaluation	. 181
	6.4.2	Kinetic Study	. 184
	6.4.3	Reusability Study	. 186
	6.4.4	Mineralization Studies	. 187
	6.4.5	Mechanistic Study	. 189
	6.4.6	Photocatalytic Performance of Other Organic Pollutants	. 192
	6.4.7	Intermediates Products and Degradation Pathway	. 193
6.5	Comparis	son study with other materials	. 195
6.6	Summary	y	. 196
СНАН	PTER 7	CONCLUSIONS AND FUTURE RECOMMENDATIONS	. 198
7.1	Conclusi	ons	. 198
7.2	Recomm	endations for Future Research	. 201
REFE	RENCES	.	. 203
APPE	NDICES		
LIST OF PUBLICATIONS			

LIST OF TABLES

	Page
Table 2.1	List of photochemical and non-photochemical AOPs (Khan <i>et al.</i> , 2022)
Table 2.2	Crystal structure of TiO ₂ (Zhang and Banfield, 2014)15
Table 2.3	Metal doping of MIL-125(Ti) and MIL-125-NH ₂ 36
Table 2.4	Combination of MIL-125(Ti) and MIL-125-NH ₂ with metal semiconductors
Table 2.5	Summary of studies on MIL-125(Ti) and MIL-125-NH ₂ as precursors derived nanocomposites for photodegradation of organic pollutants
Table 2.6	Specific properties, applications, and toxicities of various dyes (Tan <i>et al.</i> , 2015)
Table 2.7	Degradation of MB by various photocatalysts from the year 2020-present
Table 3.1	List of chemicals55
Table 4.1	Elemental analysis for N-C/TiO ₂ -Ar, N-C/TiO ₂ -N ₂ , and N-C/TiO ₂ -Air
Table 4.2	Crystallite size of the photocatalysts82
Table 4.3	Elemental analysis of the photocatalysts87
Table 4.4	Textural properties of the photocatalysts
Table 4.5	Optical properties of the photocatalysts95
Table 4.6	Percent removal at different initial concentrations and pseudo- first-order apparent constant values of N-C/TiO ₂ 900 for MB degradation
Table 4.7	Comparison of photocatalytic activity of MB over various

Table 5.1	Crystallite size of the photocatalysts	122
Table 5.2	Elemental analysis of the photocatalysts	127
Table 5.3	Textural properties of the photocatalysts	128
Table 5.4	Optical properties of the photocatalysts	135
Table 5.5	Percent removal at different initial concentrations and pseudo- first-order apparent constant values of NC/NiT900 for MB degradation	145
Table 5.6	Comparison of photocatalytic activity of MB over various photocatalyst	154
Table 6.1	Crystallite size of photocatalysts	163
Table 6.2	Elemental analysis of the photocatalysts	168
Table 6.3	Textural properties of the photocatalysts	170
Table 6.4	Optical properties of the photocatalysts	176
Table 6.5	Percent removal at different initial concentrations and pseudo-first-order apparent constant values of NC/ZnOT900 for MB degradation	185
Table 6.6	Comparison of photocatalytic activity of MB over various photocatalyst	196

LIST OF FIGURES

	Page
Figure 1.1	Crystal structure of MIL-125(Ti) consisting of eight-membered rings of Ti-oxo clusters tethered by 1,4-benzenedicarboxylates to generate a 3D structure based on fcu topology. Atom colors: Ti, blue polyhedra; C, black; O, red. H atoms are omitted for clarity (Nguyen, 2021)
Figure 2.1	Common wastewater treatment methods (Solayman et al., 2023)12
Figure 2.2	Crystal structures of TiO ₂ rutile (tetragonal, P42/mmm), brookite (orthorhombic, Pbca), and anatase (tetragonal I41/amd) polymorphs (Haggerty <i>et al.</i> , 2017)
Figure 2.3	The photocatalytic oxidation of organic compounds from textile wastewater under the UV-TiO ₂ process
Figure 2.4	Crystal structure of MIL-125(Ti). The structure can be described as a body-centered arrangement of ring-shaped $Ti_8O_8(OH)_4(-COO)_{12}$ SBUs connected by linear diatopic BDC linkers. The resulting augmented bcu net has two distinct pores corresponding to the tetrahedral and octahedral holes of a body-centered cubic packing. All hydrogen atoms are omitted for clarity. Color code: Ti , blue; C , gray; O , red (Nguyen, 2017)
Figure 2.5	Combination of MIL-125(Ti) with metal-semiconductor MIL-125(Ti) ZnO (ZnO-TF) nanorods (Xiao <i>et al.</i> , 2019)40
Figure 2.6	The molecular structure of MB dye51
Figure 3.1	Schematic diagram of the synthesized photocatalysts60
Figure 3.2	Schematic diagram of the experimental irradiation system. (a) A 45-W fluorescent lamp, (b) UV cut-off filter, (c) Glass photoreactor cell, (d) Photocatalyst, (e) MB dye solution, (f) Aeration supplied by an aquarium pump attached by a PVC tube, (g) Pasteur pipette, (h) Scissor jack and (i) Power supply

Figure 3.3	Flow diagram of research activities70
Figure 4.1	SEM images, photographs (inset), and elemental mapping of (a) Ar, (b) N ₂ , and (c) air of N-C/TiO ₂ produced by calcination at 900°C
Figure 4.2	Effect of Ar, N ₂ , and air atmosphere of N-C/TiO ₂ produced by calcination at 900°C for the photodegradation of MB dye (C_o = 50 mg L ⁻¹ , pH = 6, W = 0.4 g L ⁻¹ , t = 330 min, T = 303 K)76
Figure 4.3	Photodegradation of MB dye by N-C/TiO ₂ 300, N-C/TiO ₂ 500, N-C/TiO ₂ 700, N-C/TiO ₂ 900, and TiO ₂ ($C_o = 50 \text{ mg L}^{-1}$, pH = 6, W = 0.4 g L ⁻¹ , $t = 330 \text{ min}$, $T = 30^{\circ}\text{C}$)
Figure 4.4	XRD patterns of (a) MIL-125-NH ₂ , (b) N-C/TiO ₂ 300, (c) N-C/TiO ₂ 500, (d) N-C/TiO ₂ 700, (e) N-C/TiO ₂ 900, and (f) TiO ₂ 80
Figure 4.5	FTIR spectra of (a) MIL-125-NH ₂ (b) N-C/TiO ₂ 300, (c) N-C/TiO ₂ 500, (d) N-C/TiO ₂ 700, (e) N-C/TiO ₂ 900, and (f) TiO ₂ 83
Figure 4.6	SEM images and the corresponding particle size distributions of (a) MIL-125-NH ₂ , (b) N-C/TiO ₂ 300, (c) N-C/TiO ₂ 500, (d) N-C/TiO ₂ 700, and (e) N-C/TiO ₂ 900, (f) TiO ₂ (Magnification: $30,000 \times$)
Figure 4.7	BET adsorption-desorption isotherms of MIL-125-NH $_2$ and N-C/TiO $_2$ 900. (ADS = Adsorption, DES = Desorption)88
Figure 4.8	Thermogravimetric curve of MIL-125-NH ₂ 90
Figure 4.9	Raman spectra of MIL-125-NH ₂ , N-C/TiO ₂ 300, N-C/TiO ₂ 500, N-C/TiO ₂ 700, and N-C/TiO ₂ 900
Figure 4.10	(a) UV-vis spectra and (b) plot of $(\alpha h v)^2$ versus photon energy (hv) of MIL-125-NH ₂ , N-C/TiO ₂ 300, N-C/TiO ₂ 500, N-C/TiO ₂ 700, N-C/TiO ₂ 900, and TiO ₂
Figure 4.11	PL emission spectra of MIL-125-NH ₂ , N-C/TiO ₂ 300, N-C/TiO ₂ 500, N-C/TiO ₂ 700, N-C/TiO ₂ 900, and TiO ₂ 96

Figure 4.12	XPS spectra of N-C/TiO ₂ 900: (a) survey spectrum, high-resolution XPS spectra of (b) C 1s, (c) N 1s, (d) O 1s, and (e) Ti 2p
Figure 4.13	The effect of catalyst dosage on the removal and degradation rate, k of MB dye by N-C/TiO ₂ 900 via photocatalytic and adsorption process ($C_o = 50 \text{ mg L}^{-1}$, pH= 6, $t = 330 \text{ min}$, $T = 30 ^{\circ}\text{C}$)101
Figure 4.14	Effect of pH on MB degradation by N-C/TiO ₂ 900 under visible light irradiation. ($C_o = 50 \text{ mg L}^{-1}$, $W = 2.0 \text{ g L}^{-1}$, $t = 330 \text{ min}$, T = 30°C)
Figure 4.15	Photodegradation of MB by N-C/TiO ₂ 900 under visible light irradiation at different MB concentrations. (pH = 6, $W = 2.0$ g L ⁻¹ , $T = 30$ °C)
Figure 4.16	Photodegradation kinetics of MB on N-C/TiO ₂ 900 at different initial dye concentrations ($10-200 \text{ mg L}^{-1}$) under visible light irradiation. (pH= 6, W= 2.0 g L ⁻¹ , T= 30° C)
Figure 4.17	(a) Reusability of N-C/TiO ₂ 900 for MB degradation for five cycles of application, (b) FTIR spectra of fresh and spent N-C/TiO ₂ 900, SEM images of (c) fresh, and (d) spent N-C/TiO ₂ 900 ($C_o = 50 \text{ mg L}^{-1}$, pH= 6, W = 2.0 g L ⁻¹ , t = 330 min, t = 30°C)105
Figure 4.18	Mineralization of MB dye by N-C/TiO ₂ 900 under visible light irradiation ($C_o = 50 \text{ mg L}^{-1}$, pH = 6, $W = 2.0 \text{ g L}^{-1}$, $t = 330 \text{ min}$, $T = 30^{\circ}\text{C}$)
Figure 4.19	Effect of scavenger agents on the photocatalytic activity of N-C/TiO ₂ 900 for MB degradation under visible light ($C_o = 50 \text{ mg L}^{-1}$, pH = 6, $W = 2.0 \text{ g L}^{-1}$, $t = 330 \text{ min}$, $T = 30^{\circ}\text{C}$)
Figure 4.20	Proposed mechanism for the photodegradation of MB by N-C/TiO ₂ 900 under visible light irradiation
Figure 4.21	Photocatalytic activity of MO, OTC, 4-NP, and RWW for degradation of N-C/TiO ₂ 900. ($C_o = 50 \text{ mg L}^{-1}$, $W = 2.0 \text{ g L}^{-1}$, $t = 330 \text{ min } T = 30^{\circ}\text{C}$)

Figure 5.1	Weight percent dopant of Ni-doped MIL-125-NH ₂ for the photodegradation of MB under visible light irradiation ($C_o = 10$ mg L ⁻¹ , pH = 6, $W = 0.4$ g L ⁻¹ , $t = 330$ min, $T = 30$ °C)116
Figure 5.2	Photodegradation of MB dye by NC/NiT300, NC/NiT500, NC/NiT700, and NC/NiT900. ($C_o = 10 \text{ mg L}^{-1}$, pH= 6, W = 0.4 g L ⁻¹ , T = 30°C)
Figure 5.3	XRD patterns of (a) MIL-125-NH ₂ , (b) MNi1.0, (c) NC/NiT300, (d) NC/NiT500, (e) NC/NiT700, and (f) NC/NiT900120
Figure 5.4	FTIR spectrum of (a) MNi1.0, (b) NC/NiT300, (c) NC/NiT500, (d) NC/NiT700, and (e) NC/NiT900
Figure 5.5	SEM images and the corresponding particle size distributions of (a) MNi1.0, (b) NC/NiT300, (c) NC/NiT500, (d) NC/NiT700, and (e) NC/NiT900 (Magnification: 30,000 ×)
Figure 5.6	BET adsorption-desorption isotherms of MNi1.0 and NC/NiT900. (ADS = Adsorption, DES = Desorption)
Figure 5.7	Thermogravimetric curve of MNi1.0130
Figure 5.8	Raman spectra of MIL-125-NH ₂ , MNi1.0, NC/NiT300, NC/NiT500, NC/NiT700, and NC/NiT900
Figure 5.9	(a) UV-vis spectra and (b) plot of (αhv)² versus photon energy (hv) of MNi1.0, NC/NiT300, NC/NiT500, NC/NiT700, and NC/NiT900
Figure 5.10	PL emission spectra of MIL-125-NH ₂ , MNi1.0, NC/NiT300, NC/NiT500, NC/NiT700, and NC/NiT900136
Figure 5.11	XPS spectra of NC/NiT900: (a) survey spectrum, high-resolution XPS spectra of (b) C 1s, (c) N 1s, (d) O 1s, (e) Ti 2p, and (f) Ni 2p
Figure 5.12	The effect of catalyst dosage on the removal and degradation rate, k of MB dye by NC/NiT900 via photocatalytic and adsorption process. ($C_o = 10 \text{ mg L}^{-1}$, pH = 6, $t = 330 \text{ min}$, $T = 30^{\circ}\text{C}$)140

Figure 5.13	Effect of pH on MB degradation by NC/NiT900 under visible light irradiation. ($C_o = 10 \text{ mg L}^{-1}$, $W = 0.4 \text{ g L}^{-1}$, $t = 330 \text{ min}$, $T = 30^{\circ}\text{C}$)
Figure 5.14	Photodegradation of MB by NC/NiT900 under visible light irradiation at different MB concentrations. (pH = 6, $W = 0.4$ g L ⁻¹ , $t = 330$ min, $T = 30$ °C)
Figure 5.15	Photodegradation kinetics of MB on NC/NiT900 at different initial dye concentrations (10 – 200 mg L ⁻¹) under visible light irradiation (pH = 6, $W = 0.4$ g L ⁻¹ , $t = 330$ min, $T = 30$ °C)144
Figure 5.16	(a) Reusability of NC/NiT900 for MB degradation for five cycles of application, (b) FTIR spectra of fresh and spent NC/NiT900, SEM images of (c) fresh, and (d) spent NC/NiT900. ($C_o = 10 \text{ mg}$ L ⁻¹ , pH = 6, $W = 0.4 \text{ g L}^{-1}$, $t = 330 \text{ min}$, $T = 30^{\circ}\text{C}$)
Figure 5.17	Mineralization of MB dye by NC/NiT900 under visible light irradiation. ($C_o = 10 \text{ mg L}^{-1}$, pH = 6, $W = 0.4 \text{ g L}^{-1}$, $t = 330 \text{ min}$, $T = 30^{\circ}\text{C}$)
Figure 5.18	Effect of scavenger agents on the photocatalytic activity of NC/NiT900 for MB degradation under visible light. ($C_o = 10 \text{ mg}$ L ⁻¹ , pH = 6, $W = 0.4 \text{ g L}^{-1}$, $t = 330 \text{ min}$, $T = 30^{\circ}\text{C}$)
Figure 5.19	Proposed mechanism for the photodegradation of MB by NC/NiT900 under visible light irradiation
Figure 5.20	Photocatalytic activity of MO, OTC, 4-NP, and RWW for degradation of NC/NiT900 ($C_o = 10 \text{ mg L}^{-1}$, $W = 0.4 \text{ g L}^{-1}$, $t = 330 \text{ min}$, $T = 30^{\circ}\text{C}$)
Figure 6.1	Effect of Zn wt% on the photocatalytic performance of Zn/MIL-125-NH ₂ for the photodegradation of MB ($C_o = 50 \text{ mg L}^{-1}$, pH = 6, $W = 0.4 \text{ g L}^{-1}$, $t = 330 \text{ min}$, $T = 30^{\circ}\text{C}$)
Figure 6.2	Photodegradation of MB dye by NC/ZnOT300, NC/ZnOT500, NC/ZnOT700 and NC/ZnOT900 under visible light irradiation $(C_0 = 50 \text{ mg L}^{-1} \text{ pH} = 6 W = 0.4 \text{ g L}^{-1} t = 330 \text{ min } T = 30^{\circ}\text{C})$ 159

Figure 6.3	XRD patterns of (a) 1ZnM (b) NC/ZnOT300 (c) NC/ZnOT500 (d) NC/ZnOT700 (e) NC/ZnOT900 (f) ZnO
Figure 6.4	FTIR spectra of (a) ZnO (b) 1ZnM (c) NC/ZnOT300 (d) NC/ZnOT500 (e) NC/ZnOT700, and (f) NC/ZnOT900164
Figure 6.5	SEM images and particle size distribution of (a) ZnO (inset: 2000 × magnification) (b) 1ZnM (c) NC/ZnOT300 (d), NC/ZnOT500 (e), NC/ZnOT700 (f), NC/ZnOT900 (Magnification: 30,000 ×)167
Figure 6.6	BET adsorption-desorption isotherms of 1ZnM and NC/ZnOT900. (ADS = Adsorption, DES = Desorption)169
Figure 6.7	Thermogravimetric curve of 1ZnM
Figure 6.8	Raman spectra of 1ZnM, NC/ZnOT300, NC/ZnOT500, NC/ZnOT700, and NC/ZnOT900
Figure 6.9	(a) UV-vis spectra and (b) plot of (<i>αhv</i>) ² versus photon energy (<i>hv</i>) of ZnO, 1ZnM, NC/ZnOT300, NC/ZnOT500, NC/ZnOT700, NC/ZnOT900
Figure 6.10	PL emission spectra of ZnO, 1ZnM, NC/ZnOT300, NC/ZnOT500, NC/ZnOT700, NC/ZnOT900
Figure 6.11	XPS spectra of NC/ZnOT900: (a) survey spectrum, high-resolution XPS spectra of (b) C 1s, (c) N 1s, (d) O 1s, (e) Ti 2p, and (f) Zn 2p
Figure 6.12	The effect of catalyst dosage on the removal efficiency and degradation rate, k of MB dye by NC/ZnOT900 via photocatalytic and adsorption process ($C_o = 50 \text{ mg L}^{-1}$, pH = 6, $t = 330 \text{ min}$, $T = 30 ^{\circ}\text{C}$)
Figure 6.13	Effect of pH on MB degradation by NC/ZnOT900 under visible light irradiation ($C_o = 50 \text{ mg L}^{-1}$, $W = 2.0 \text{ g L}^{-1}$, $t = 330 \text{ min}$, $T = 30^{\circ}\text{C}$)
Figure 6.14	Photodegradation of MB by NC/ZnOT900 under visible light irradiation at different MB concentrations (pH = 6, $W = 2.0$ g L ⁻¹ , $T = 30$ °C)

Figure 6.15	Photodegradation kinetics of MB on NC/ZnOT900 at different initial dye concentrations (10 – 200 mg L ⁻¹) under visible light irradiation (pH = 6, $W = 2.0$ g L ⁻¹ , $t = 330$ min, $T = 30$ °C)185
Figure 6.16	(a) Reusability of NC/ZnOT900 for MB degradation for five cycles of application, (b) FTIR spectra of fresh and spent NC/ZnOT900, SEM images of (c) fresh and (d) spent NC/ZnOT900. ($C_o = 50 \text{ mg L}^{-1}$, pH = 6, $W = 2.0 \text{ g L}^{-1}$, $t = 330 \text{ min}$, $T = 30 ^{\circ}\text{C}$)
Figure 6.17	Mineralization of MB dye by NC/ZnOT900 under visible light irradiation ($C_o = 50 \text{ mg L}^{-1}$, pH = 6, $W = 2.0 \text{ g L}^{-1}$, $t = 330 \text{ min}$, $T = 30^{\circ}\text{C}$)
Figure 6.18	Effect of scavenger agents on the photocatalytic activity of NC/ZnOT900 for MB degradation under visible light ($C_o = 50$ mg L ⁻¹ , pH = 6, $W = 2.0$ g L ⁻¹ , $t = 330$ min, $T = 30$ °C)
Figure 6.19	Proposed mechanism for the photodegradation of MB by NC/ZnOT900 under visible light irradiation
Figure 6.20	Photocatalytic activity of MO, OTC, 4-NP, and RWW for degradation of NC/ZnOT900 ($C_o = 50 \text{ mg L}^{-1}$, $W = 2.0 \text{ g L}^{-1}$, $t = 330 \text{ min}$, $T = 30^{\circ}\text{C}$)
Figure 6.21	Possible pathway of MB dye by NC/ZnOT900

LIST OF SYMBOLS

Å Angstrom

θ Theta

 λ Wavelength

cm Centimeter

eV Electron volt

g Gram

g L⁻¹ Gram per liter

h Hours

M Molar

min Minutes

 $mg L^{-1}$ Milligram per liter

nm Nanometer

μm Micrometer

s Second

t Time

T Temperature

W Watt

LIST OF ABBREVIATIONS

4-NP 4-nitrophenol

BET Brunauer – Emmett – Teller

CB Conduction band

C_o Initial concentration

C_t Concentration at time t

CP Carbon porous

e⁻ Electron

E_g Energy band gap

FTIR Fourier Transform Infra-Red

h Plank constant

h⁺ Holes

IUPAC International Union of Pure and Applied Chemistry

JCPDS Joint Committee on Powder Diffraction Standards

 k_{app} Apparent first-order rate constant

 K_{LH} Adsorption coefficient of the reactant

 k_r Reaction rate constant

kV Kilo volt

LH Langmuir-Hinshelwood

MB Methylene blue

MIL Material of Lavoisier

MIL-125-NH₂ Material of Lavoisier-125-amine

MO Methyl orange

NCP Nitrogen-doped Carbon Porous

NH₂BDC 2-aminoterepthalic acid

OTC Oxytetracycline

 pH_{pzc} pH of point zero charge

RWW Real wastewater

TGA Thermogravimetric analysis

TOC Total organic carbon

UV Ultraviolet

UV-Vis/DRS Ultraviolet-visible diffuse reflectance spectroscopy

 $\begin{array}{ccc} VB & & Valence \ band \\ V_os & & Oxygen \ vacancy \\ wt\% & & Weight \ percent \end{array}$

XPS X-Ray photoelectron spectroscopy

XRD X-Ray diffraction

LIST OF APPENDICES

Appendix A	Calculations of CB and VB level
Appendix B	Kinetics Study
Appendix C	EDX mapping of (a) MIL-125-NH ₂ , (b) N-C/TiO ₂ 300, (c) N-
	C/TiO ₂ 500, (d) N-C/TiO ₂ 700, (e) N-C/TiO ₂ 900
Appendix D	EDX mapping of (a) MNi1.0, (b) NC/NiT300, (c) NC/NiT500,
	(d) NC/NiT700, and (e) NC/NiT900.
Appendix E	EDX mapping of (a) 1ZnM (b) NC/ZnOT300 (c) NC/ZnOT500
	(d) NC/ZnOT700 (e) NC/ZnOT900
Appendix F	Mass spectra of photodegradation of MB starting from blank to
	330 min

KERANGKA ORGANIK LOGAM BERASASKAN TITANIUM DAN PENGUBAHSUAIANNYA OLEH PENGURAIAN TERMAL UNTUK AKTIVITI PEMFOTOMANGKIN SINARAN CAHAYA NAMPAK

ABSTRAK

Pada masa ini, suatu templat baharu untuk mensintesis bahan organik/tak organik yang membentuk struktur karbon berpori dengan keliangan hierarki telah menjadi tumpuan penyelidik. Bahan berliang karbon daripada kerangka logamorganik (MOF) mempunyai luas permukaan yang besar tetapi menghadapi cabaran dengan struktur yang didominasi oleh mikropori, aglomerasi tak terbalik nanopartikel logam, dan kawalan terhad terhadap transformasi struktur. Kajian ini dibahagikan kepada tiga bahagian. Pertama, MIL-125-NH₂ disediakan menggunakan kaedah solvotermal dengan aliran gas lengai yang tetap untuk mewujudkan keadaan lengai. Kemudian, MIL-125-NH₂ dikalsin pada pelbagai suhu di bawah atmosfera lengai (gas argon) untuk menghasilkan titanium dioksida berliang karbon terdop nitrogen (N-C/TiO₂). Mengikuti prosedur yang sama, dua modifikasi berbeza komposit yang terdop Ni dan ZnO disediakan dengan mengubah peratus berat (wt%). Komposit terdop Ni (NC/NiT), dan ZnO (NC/ZnOT) dihasilkan dengan mengekalkan peratus berat optimum kedua-dua modifikasi melalui suhu kalsinasi yang berbeza di bawah gas argon. Sifat kimia, fizikal dan optik bahan yang disintesis disiasat dengan pelbagai kaedah pencirian. Kalsinasi N-C/TiO₂ dijalankan di bawah tiga atmosfera yang berbeza (argon, nitrogen, dan udara). Menariknya, didapati bahawa gas argon tidak hanya mengekalkan bentuk ortorombik MIL-125-NH₂ pada suhu kalsinasi tinggi tetapi juga menunjukkan fotodegradasi yang lebih tinggi untuk metilena biru (MB). Penukaran fasa anatas amorfus kepada rutil kristalin direkodkan

ketika suhu kalsinasi meningkat dari 300-900°C. Aktiviti pemfotomangkin N-C/TiO₂900 ditingkatkan oleh kekosongan oksigen dan kecacatan logam. Ciri-ciri ini mengecilkan tenaga jurang jalur dan mengurangkan penggabungan semula pasangan electron-lubang yang dihasilkan secara foto. Penggabungan Ni sebagai dopan dalam MIL-125-NH₂ meningkatkan prestasi pemfotomangkinnya dengan memudahkan pemisahan cas melalui penangkapan elektron yang berkesan. Selepas sampel dikalsin pada pelbagai suhu, NC/NiT900 berubah menjadi fasa rutil kristalin yang menghasilkan fotodegradasi tertinggi. Penyelidikan lanjut menunjukkan bahawa kehadiran Ni mengurangkan jurang jalur dan memendekkan komponen hayat fotopendarcahaya (PL), menghasilkan pemindahan cas yang lebih baik. Kehadiran ZnO sebagai komposit membentuk heterosimpangan untuk pemisahan pembawa cas yang efisyen. Seperti NC/NiT, NC/ZnOT900 telah berubah menjadi fasa kristalin rutil. Struktur morfologi MIL-125-NH2 dengan Zn menyerupai sel darah putih dengan struktur berdendritik dengan saiz purata 1378 nm. Analisis spektroskopi fotoelektron sinar-X (XPS) menunjukkan bahawa Zn wujud sebagai fasa ZnO yang berasingan yang mengesahkan komposit ZnO/TiO₂. Prestasi pemfotomangkin ketigatiga sampel berada dalam urutan berikut: NC/ZnOT900 (96.8%) > NC/NiT900 (96.0%) > N-C/TiO₂900 (93%). Kadar mineralisasi untuk NC/ZnOT900 lebih tinggi berbanding NC/TiO₂900 dan NC/NiT900 dengan 86.7% selepas 330 minit. Radikal hidroksil dan superoksida adalah spesies reaktif yang paling penting untuk semua sampel yang dioptimumkan. Selain itu, N-C/TiO₂900 (64.2%), NC/NiT900 (70.0%), dan NC/ZnOT900 (86.2%) telah menunjukkan sebagai fotomangkin yang efektif dan boleh dipercayai setelah digunakan semula selama lima kitaran. Keputusan kajian ini memperluaskan pengetahuan tentang mentransformasikan MIL-125-NH₂ yang dikalsin pada suhu tinggi bagi menghasilkan N-C/TiO₂. Kejayaan penyelidikan ini

membuka laluan untuk pelbagai aplikasi, termasuk pemfotomangkinan, penjerapan, penderiaan kimia, pemangkinan, penyimpanan dan penukaran tenaga dan pengekstrakan fasa pepejal.

TITANIUM-BASED METAL-ORGANIC FRAMEWORK AND ITS MODIFICATIONS BY THERMAL DECOMPOSITION FOR VISIBLE LIGHT PHOTOCATALYTIC ACTIVITY

ABSTRACT

Currently, a new template for synthesizing organic/inorganic material that creates porous carbon structures with hierarchical porosity has become the attention of researchers. Carbon porous materials from metal-organic frameworks (MOFs) have a large surface area but face challenges with a micropore-dominated structure, irreversible metal nanoparticle agglomeration, and limited control over structural transformation. This study is divided into three sections. Firstly, MIL-125-NH₂ was prepared using a solvothermal method with a constant inert gas flow to create an inert condition. Then, MIL-125-NH₂ was calcined at various temperatures under an inert atmosphere (argon gas) to produce nitrogen-doped carbon porous titanium dioxide (N-C/TiO₂). Following the same procedure, two different modifications of Ni-doped and ZnO composites were prepared by varying the weight percentage (wt%). Ni-doped (NC/NiT), and ZnO composites (NC/ZnOT) were produced by subjecting the optimal wt% of both modifications through different calcination temperatures under argon gas. The chemical, physical, and optical properties of the synthesized materials were investigated by various characterization methods. The calcination of N-C/TiO₂ was performed under three different atmospheres (argon, nitrogen, and air). Remarkably, it was observed that argon gas not only maintained the orthorhombic shape of MIL-125-NH₂ at high calcination temperatures but also demonstrated higher photodegradation for methylene blue (MB). The phase conversion of amorphous anatase to crystalline rutile was recorded as the calcination

temperature increased from 300-900°C. The photocatalytic activity of N-C/TiO₂900 was enhanced by oxygen vacancies and metal defects. These features narrowed the band gap energy and reduced the photogenerated electron-hole pair recombination. The incorporation of Ni as a dopant in MIL-125-NH₂ enhances its photocatalytic performance by facilitating charge separation through effective electron capture. After the sample was calcined at various temperatures, NC/NiT900 converted to a crystalline rutile phase that resulted in the highest photodegradation. Further investigation demonstrates that the presence of Ni reduces the band gap and shortens the photoluminescence lifetime components, leading to improved charge transfer. The presence of ZnO as a composite forms heterojunctions for efficient charge carrier separation. Like NC/NiT, NC/ZnOT900 has transformed into a rutile crystalline phase. The morphological structure of MIL-125-NH₂ with Zn resembles white blood cells with a dendritic-like structure with an average size of 1378 nm. Xray photoelectron spectroscopy (XPS) analysis reveals that Zn exists as a separate ZnO phase which confirms the composite of ZnO/TiO₂. The photocatalytic performance of all three samples was in the following order: NC/ZnOT900 (96.8%) > NC/NiT900 (96.0%) > N-C/TiO₂900 (93.0%). The mineralization rate for NC/ZnOT900 was higher compared to N-C/TiO₂900 and NC/NiT900 with 86.7% after 330 min. Hydroxyl and superoxide radicals were the most important reactive species for all the optimized samples. Additionally, N-C/TiO₂900 (64.2%), NC/NiT900 (70.0%), and NC/ZnOT900 (86.2%) were demonstrated to be effective and reliable photocatalysts after being reused for five cycles. The result of this study extends the knowledge of transforming highly calcined MIL-125-NH₂ at high temperatures into developing N-C/TiO₂. The research success offers a pathway for various applications, including photocatalysis, adsorption, chemical sensing, catalysis, energy storage and conversion, and solid-phase extraction.

CHAPTER 1

INTRODUCTION

1.1 Research Background

The 2030 Agenda for Sustainable Development Goal 6 (SDG 6) emphasizes the need to provide every human population with water and sanitary facilities that are managed sustainably by the year 2030 (Ortigara et al., 2018). In addition to drinking water, SDG 6 addresses technology for water harvesting, water efficiency, desalination, wastewater treatment, recycling, and reuse. However, human and industrial activities, such as population growth, high energy demand, and improper product disposal, have recently become more prevalent. As a result, there were serious pollution issues, including groundwater and river contamination. The outcome has had negative environmental effects that may impact the entire ecosystem (Singh et al., 2022). Water is used every day for domestic, agricultural, or industrial, and it discharges effluent containing undesirable pollutants that can be toxic (Crini and Lichtfouse, 2019). The presence of carcinogenic and toxic substances in effluents released into the water stream has raised serious concerns among humans (Shabir et al., 2022). Furthermore, the discharge of industrial effluents often includes synthetic dyes, which are recognized as a significant and hazardous pollutant due to their potential toxicity and carcinogenicity, posing additional challenges to achieving sustainable water quality under SDG 6.

Therefore, searching for efficient and effective techniques to address these issues is crucial. Much research on the use of visible light for environmental remediation applications such as water decontamination has been underway for years. An advanced oxidation process (AOP) application in semiconductor-based photocatalysis has been identified as an effective solution for degrading recalcitrant

molecules. The growing interest in heterogeneous photocatalysis for water purification has led to the designing, creation, and modification of a variety of photocatalysts. Heterogeneous photocatalysis using metal oxides as semiconductors, such as TiO₂, WO₃, CdS, and ZnO, has risen in popularity. This is due to its benefits, which include the ability to function at room temperature and pressure, low cost, and environmentally friendly nature. The most widely used photocatalyst in the photodegradation of water contaminants is titanium dioxide (TiO₂) due to its efficient photocatalytic activity, chemical stability, and low biological toxicity. However, pure TiO₂ still has low photocatalytic effectiveness because of its large band gap energy, which makes it more likely to excite under UV light, and a high recombination rate of electron-hole pairs (Chairungsri *et al.*, 2022).

To increase the photocatalytic performance and the utilization of visible light, various modification strategies, such as semiconductor coupling (Lu *et al.*, 2018), transition metallic/non-metallic doping (Etacheri *et al.*, 2015, Liao *et al.*, 2017), self-assembly (Zhang *et al.*, 2015), and template preparation (Zhou *et al.*, 2018), have been developed. The degradation performance of the photocatalysts is hindered by limitations, including the agglomeration of TiO₂ nanoparticles, which leads to the inaccessibility of the photocatalytic active sites. Various methods have been developed by compositing TiO₂ with various types of carbon materials, such as graphene or activated carbon, to increase the accessibility of the active sites and prevent the formation of agglomerates. The pore sizes and shapes of photocatalysts with high surface area are the key components to removing organic pollutants. Therefore, the template method stands out among the various synthetic techniques that have been established in recent years to prepare novel porous carbon structures with hierarchical porosity and new properties. This method involves the

establishment an organic-inorganic template composite and removal of the inorganic template by carbonization.

Researchers have recently explored metal-organic framework (MOF) as a new strategy to develop a distinctive structure with a highly ordered pore structure and large surface area (Hu et al., 2020). Furthermore, when exposed to light, these porous crystalline materials function as semiconductors, and allow them to harvest light similarly to photocatalysts. MOFs, otherwise classified as porous coordination polymers (PCPs), are a type of porous crystalline hybrid material made up of metallic ions or clusters called secondary building units (SBUs), and connected with multidentate organic linkers that are bound by moderate force coordination bonds (Nasalevich et al., 2014). In the last decade, an increasing interest in MOFs has been developed in chemistry and related fields due to their ability to alter structural and functional parameters. MOFs are appealing due to their varied nature and unique characteristics. MOFs have emerged as a functional material with accessible components such as crystalline nature, tuneable porosity, large surface area, pore volumes, uniform pore size, excellent optoelectronic properties, and high thermal and mechanical stabilities (Yaghi et al., 2003). Furthermore, the organic properties present in the MOF can harvest light and possibly in the visible region, activating the inorganic nodes (Dhakshinamoorthy et al., 2016). Furthermore, MOFs can integrate within the voids guests and can improve the efficiency of the material by serving as charge carrier reservoirs or co-catalysts (Dhakshinamoorthy et al., 2016). As a result, MOFs can be used as photocatalysts in various ways, given that the material has sufficient photostability.

Material Institute Lavoisier-125 (MIL-125(Ti)), a titanium-based MOF with a chemical structure of $Ti_8O_8(OH)_4(O_2C-C_6H_4-CO_2)_6$, has interestingly high stability

and photocatalytic activity as displayed in Figure 1.1. The Ti₈O₈ ring that acts as an inorganic building unit is made up of a cyclic octamer of TiO₆ octahedra sharing corners, with each octahedron of the octameric unit attached to terephthalate linkers to form 12 connected SBUs (Hendon *et al.*, 2013). The eight rings are arranged in a cubic-centered packing pattern, and the overall structure is simplified into a face-centered cubic (**fcu**) topology. MIL-125(Ti) can be classified into two types of cages: distorted octahedral and tetrahedral (Vaesen *et al.*, 2013). The performance of MIL-125(Ti) was far from ideal, although it was first recorded with a photocatalytic ability (Dan-Hardi *et al.*, 2009). MIL-125(Ti) is photoactive only by UV irradiation with an optical band gap of ca. 3.6 eV. The band gap is a fundamental factor for photocatalysts, representing the lowest energy required to produce an electron-hole charge carrier.

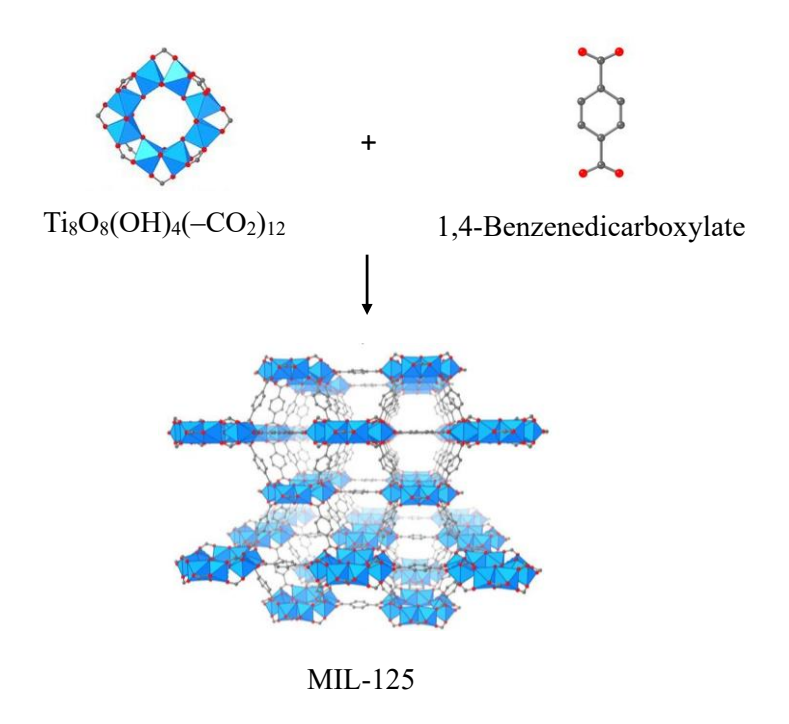


Figure 1.1 Crystal structure of MIL-125(Ti) consisting of eight-membered rings of Ti-oxo clusters tethered by 1,4-benzenedicarboxylates to generate a 3D structure based on fcu topology. Atom colors: Ti, blue polyhedra; C, black; O, red. H atoms are omitted for clarity (Nguyen, 2021)

Functionalizing the organic linker (terephthalic acid) with amine groups (2-aminoterephthalic acid) may narrow the band gap, improving light absorption and expanding optical absorption from 350 to 550 nm (Bedia *et al.*, 2019). For example, amine-functionalized MIL-125(Ti) (MIL-125-NH₂) was later synthesized that consists of six linkers and a metal cluster. The chemical formula of MIL-125-NH₂ is Ti₈O₈(OH)₄(2OC-NH₂-C₆H₃-CO₂)₆·18(CH₃OH)·3((CH₃)₂NCHO) (Zlotea *et al.*, 2011, Zhang *et al.*, 2019a). The nitrogen sorption analysis reveals that MIL-125-NH₂ is highly porous with a micropore volume of 0.72 cm³ g⁻¹. MIL-125-NH₂ has become an attractive material due to its large BET surface area of 1730 m² g⁻¹ (Vaesen *et al.*, 2013). Apart from that, the structure's intramolecular hydrogen bonding between the aromatic amino hydrogen atoms and carboxylate oxygen atoms makes MIL-125-NH₂ more resistant to moisture than MIL-125(Ti) (Zhu *et al.*, 2018). The high thermal and chemical stability of MIL-125-NH₂ has made it a promising material for a variety of applications (Yue *et al.*, 2021).

Thus, scientific efforts have been conducted to convert Ti-MOF into TiO₂ where metal and oxygen atoms are organized at the periodic atom level within Ti-MOF crystals. Therefore, it allows the Ti-MOF to be entirely transformed into metallic oxides without long-range atomic migration while retaining a certain degree of permanent porosity via thermal treatment (Gao *et al.*, 2014, Zhang and Lin, 2014). Organic linkers are transformed into a carbon porous structure by carbonization at high temperatures under an inert atmosphere, and the metallic component is distributed within this carbonaceous structure in the form of metal or metal oxide nanoparticles. The carbon porous materials formed during the conversion process typically exhibit high thermal stability (Yang *et al.*, 2019b). It helps maintain the structural integrity of the material during thermal treatment, preventing the collapse

or agglomeration of nanoparticles. Depending on the gas atmosphere, the resulting nanocomposites can preserve the inherited morphologies of MOF precursors. A previous report stated that changes in physicochemical parameters through the calcination process may generate a large surface area with an appropriate micropore/mesopore ratio, in strengthening separation and migration rates of photogenerated charge (Chen *et al.*, 2020). Most importantly, the precursor's large surface area and crystallinity are preserved in this highly thermal treatment which also exhibits certain unique traits like exceptional rate capabilities and extraordinary photocatalytic potential.

Besides, the carbon porous materials derived from Ti-based MOF produce a lower band gap and reduced photogenerated electron-hole that resulted in higher photodegradation performance (Zheng et al., 2021). Moreover, the introduction of metal dopants such as nickel encourages the separation of photogenerated electrons and holes and increases quantum efficiency (He et al., 2021, Valero-Romero et al., 2019, Ao et al., 2018, Nasalevich et al., 2015). Additionally, more oxygen can be produced when metal is incorporated into the MOF structure, thus reducing the band gap, which eventually will enhance photocatalytic activity (Gao et al., 2020). Apart from that, the composites of two dissimilar semiconductors, such as ZnO, provide adequate mineralization where the charge carriers can be transferred transversely on the heterostructures by directing these charge carriers to different materials via a junction (Marschall, 2014). This allows the electrons and holes to spend more time apart, enough for reduction and oxidation. Other than decreasing the recombination rate, heterojunctions are formed to improve the efficiency of semiconductors by redshifting the light absorption (Linsebigler et al., 1995).

1.2 Problem Statements

Titania is a material with great potential in many applications due to its accessibility and biocompatible qualities. However, TiO₂ has a large band gap energy (ca. 3.2 eV) and a small surface area. Apart from that, the commonly synthesized TiO₂ results in low crystallite size and surface area. Moreover, the high recombination rates further limit their activity. Numerous initiatives have been made to address the drawbacks of TiO₂ including doping with metal or non-metal species, the creation of heterojunctions, and the production of defects (Jedidi et al., 2022, Khedr et al., 2017, Liu and Perng, 2020). However, the photodegradation performance of the photocatalysts is inevitably constrained by other issues, such as the inaccessibility of the photocatalytic active sites caused by the formation of agglomerates of TiO₂ nanoparticles (Ribao et al., 2017, Brindha and Sivakumar, 2017, Xu et al., 2016). In order to address these challenges, various approaches have been utilized to combine TiO₂ with carbon materials like graphene or activated carbon (Veeresh et al., 2023). The combination made by physical and mechanical mixing methods typically has an uneven distribution of metal oxides on graphitic carbon and poor textural properties with only a minimal improvement in photocatalytic performance. A prospective and effective photocatalyst should exhibit adjustable surface, optical, and textural characteristics. Pore shapes and sizes as well as large surface area play an important role in serving as a beneficial feature to eliminate organic pollutants. Attempts have been undertaken to transform Ti-based MOF into TiO₂, arranging Ti and O atoms at the atomic level. Compared with other conventional thermal treatments, carbon porous materials derived from Ti-based MOFs have a larger specific surface area and a more diversified pore structure (Li et al., 2017b). However, the high thermal treatment causes the breakdown of the chemical structure which leads to surface agglomeration. Therefore, with proper thermal treatment under different inert atmospheric conditions, the organic ligand can be transformed into carbon porous metal oxide TiO₂ and distributed uniformly in the material as well as preserving the morphological structure.

Unfortunately, detailed studies on TiO₂ derived from MIL-125-NH₂ and the influence of different inert gases are still lacking. Moreover, there is limited work reported on the phase transition of nitrogen-doped carbon porous materials derived from MIL-125-NH₂ with the modification of Ni-doped and ZnO composites using one-pot synthesis. Therefore, it is necessary to investigate highly calcined MIL-125-NH₂ and its modifications through one-step calcination under an inert atmosphere.

1.3 Research Objectives

The main objectives of this work are:

- 1. To synthesize N-C/TiO₂, NC/NiT, and NC/ZnOT composite via solvothermal method under an inert gas atmosphere at different calcination temperatures.
- 2. To characterize the as-prepared photocatalysts for their physical, chemical, and optical properties.
- To evaluate the photocatalytic performance and reaction kinetics of the photocatalysts for the degradation of methylene blue under visible light irradiation.
- 4. To investigate the reusability and the effectiveness of the photocatalysts through mineralization study.
- 5. To explore the underlying mechanisms of the optimized photocatalyst by determining the active species involved in the photocatalytic reaction.

1.4 Scope of Research

This study is intended to investigate the effect of various atmospheric conditions on MIL-125-NH₂, the addition of Ni²⁺ as a metal dopant, and ZnO as heterostructure composites producing nitrogen-doped carbon porous TiO₂ and their photocatalytic performance on methylene blue (MB). This thesis is divided into seven chapters:

Chapter 1 is an overview of the study. This chapter briefly explains the background of the study, the problem statement, and the objectives of this research.

Chapter 2 provides a comprehensive literature review and thorough assessment of the fundamentals of wastewater treatment, photocatalysis, metalorganic framework (MOF) properties, and its modification. Comprehensive analysis of the impact of dyes as organic pollutants with an emphasis on MB.

Chapter 3 describes the materials and methods used for this study. The preparation and synthesis method of each modification was fully described. This chapter also covers the morphology, spectroscopy, and optical characterization of the prepared photocatalyst. Finally, a description of the experimental methods used in photodegradation was provided.

Chapter 4 discussed in detail the effect of different atmospheric conditions, and calcination temperatures of nitrogen-doped carbon porous TiO₂ derived from MIL-125-NH₂. Characterization, photocatalytic activity, reusability, mineralization study, and mechanistic study were discussed thoroughly. The effectiveness of the prepared photocatalyst was done by comparing it with other organic pollutants.

Chapters 5 and 6 cover in-depth the addition of Ni^{2+} and ZnO on MIL-125-NH₂ and the effect of calcination temperature producing nitrogen-doped carbon

porous TiO_2 in each respective chapter. The characterization, photocatalytic activity, and mineralization study were comprehensively elaborated. Investigation of other organic pollutants was done to assess the efficiency of the optimized photocatalyst.

Chapter 7 concludes the presented information and provides recommendations for future works.

CHAPTER 2

LITERATURE REVIEW

2.1 Wastewater Treatment Method

Due to scientific advancements and a growing body of knowledge, wastewater treatment has started to pay more attention to the health risks associated with the release of toxic and potentially toxic chemicals into the environment. There are three different types of water treatment: physical, chemical, and biological treatment. Physical treatment methods include membrane filtration, reverse osmosis, electrolysis, and adsorption. The primary issue with membrane technology is its limited life owing to fouling, which needs frequent maintenance (Thamaraiselvan and Noel, 2015). As a result, periodic chemical cleaning and replacement costs must be included while determining its economic viability. Due to its ease of use and relatively low application cost, adsorption is a promising method with significant potential in the decolorization process (Ramutshatsha-Makhwedzha Nomngongo, 2022). Activated carbon is commonly associated with the adsorption technique (Azam et al., 2022). However, its application is limited because activated carbon is expensive; therefore, advancements in research and regeneration are required (Husien et al., 2022).

On the other hand, the principal agents employed in the chemical treatment of wastewater are coagulants and flocculants (El-Gaayda *et al.*, 2021). It is performed by introducing chemicals into the effluent, such as ferric ions, aluminum, and calcium, to produce flocs. Even though the chemical process is the most affordable and effective, the primary drawback would be chemical expenses are substantial and the market prices change frequently according to demand and manufacturing costs (Bal and Thakur, 2022). Biological treatment is more economical than physical and

chemical approaches. Although microorganisms can acquire and degrade numerous pollutants, their applications are typically restricted by technical constraints (Singh *et al.*, 2022). Furthermore, some published articles stated that with current conventional technology, the biological restoration procedure is inefficient at accomplishing good color removal (Hamad and Idrus, 2022). Figure 2.1 summarizes the chemical, physical, and biological treatments (Anjaneyulu *et al.*, 2019). Among these wastewater treatment methods, the advanced oxidation process (AOP) has gained a lot of interest. It uses a combination of UV irradiation, catalysts, and oxidants to generate hydroxyl radicals (•OH) in solutions to eliminate hazardous organic substances in wastewater.

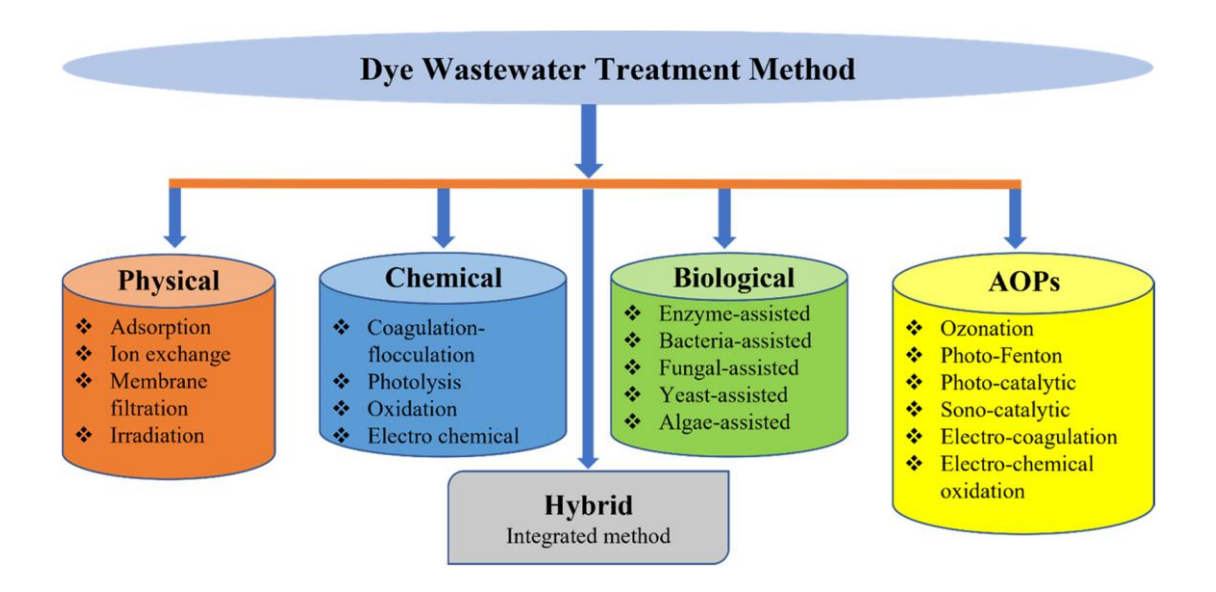


Figure 2.1 Common wastewater treatment methods (Solayman et al., 2023)

2.2 Advanced Oxidation Process (AOP)

Advanced oxidation processes (AOPs) are a group of oxidative water treatments used to remediate toxic effluents that have been growing in the wastewater management industry. UV/O₃, UV/H₂O₂, Fenton, photo-Fenton, nonthermal plasmas, sonolysis, photocatalysis, supercritical water oxidation processes, and others are examples of AOPs that are presented in Table 2.1.

Table 2.1 List of photochemical and non-photochemical AOPs (Khan *et al.*, 2022)

Non-photochemical AOPs	Photochemical AOPs	
Ozone (O ₃)	Photolysis $(UV + H_2O_2)$	
Fenton ($Fe^{2+} + H_2O_2$)	Photo-Fenton (Solar Light + Fenton)	
Electrolysis (Electrodes + Current)	Photocatalysis (Light + Catalyst)	
$Microwave + H_2O_2$		

AOPs are generally used in water and wastewater to eliminate organic and inorganic pollutants as it acts as a powerful oxidizing agent in the form of hydroxide (OH) but more precisely, its neutral variant, the hydroxyl radical (•OH) (Wang and Wang, 2020). Five main advantages of AOPs that have been reported are: (1) markedly decreased levels of inorganic and organic substances, (2) organic pollutants are completely mineralized to carbon dioxide, water, and mineral salts, 3) produces non-toxic by-products while avoiding the discharge of secondary pollutants, 4) strong reactivity and non-selectivity of hydroxyl radicals towards contaminants, 5) applications for wastewater treatment or pre-treatment (Wang *et al.*, 2020a). Ozone (O₃), hydrogen peroxide (H₂O₂), and ultraviolet radiation (UV) are typically employed to produce enough •OH to degrade organic contaminants in a variety of

combinations. Usually, AOPs may reduce the pollutants from several hundred ppm to less than 5 ppb when applied under correctly tuned settings. These radicals are non-selective, which means they target practically all organic compounds and react quickly. The pollutants create intermediates after being degraded by the •OH radical. These •OH radicals react with the dissolved pollutants, triggering a chain of oxidation processes that eventually mineralize the contaminants into CO₂, H₂O, and inorganic ions. Light-driven AOPs such as photocatalysis (light + catalyst) are the most appealing approach for wastewater treatment due to their low cost and high efficiency.

2.3 Photocatalysis

Photocatalytic reactions occur in both homogeneous and heterogeneous environments. Homogeneous photocatalysis is a process that occurs during the same phase as the reactant and photocatalyst. Homogeneous photocatalysis consists of a group of soluble molecular catalysts that incorporate a light-absorbing substance (photosensitizer) as well as catalytic sites for oxidation and reduction processes (solution) (Saini and Ratan, 2022). For homogeneous photocatalysis, dyes display an intensive band in UV and visible ranges. However, disadvantages such as poor recovery, instability, and potential toxicity limit their application. For these reasons, heterogeneous photocatalysis has received greater attention due to its potential use in numerous chemical, environmental, and energy-related applications (Nunzi and De Angelis, 2022). The growing interest in heterogeneous photocatalysis for water purification research has resulted in the design and creation of a wide range of photocatalysts and their derivatives. Heterogeneous photocatalysis using metal oxides as semiconductors, such as TiO₂, WO₃, CdS, and ZnO, has risen in popularity

because of its advantages, for example, the ability to operate at room temperature and pressure. Apart from that, they are environmentally friendly and have a low energy band gap, making them suitable for various effluent treatment applications, including organic contaminants present in real wastewater (Deng and Zhao, 2015). Among them, TiO₂ is the most studied catalyst because it is a chemically stable, non-toxic, and inexpensive photocatalyst (Gopinath *et al.*, 2020).

2.3.1 Titanium Dioxide (TiO₂)

Titanium dioxide exhibits three primary crystalline structures: anatase (tetragonal), rutile (tetragonal), and brookite (orthorhombic). The properties of these crystal structures are illustrated in Table 2.2. Although the octahedral structures of these minerals are identical, their assembly patterns and deformation allow for their differentiation. Octahedral anatase crystals, despite sharing a tetragonal structure with rutile, can be distinguished by their vertices and are slightly elongated along the vertical axis, as depicted in Figure 2.2.

Table 2.2 Crystal structure of TiO₂ (Zhang and Banfield, 2014)

Properties	Rutile	Anatase	Brookite
Structures	Tetragonal crystal lattice	Tetragonal crystal lattice	Orthorhombic crystal lattice
Lattice parameters	a = 4.5941 Å, b = 4.5941 Å and c = 2.9589 Å	a = 3.7842 Å, b = 3.7842 Å and c = 9.5146 Å	a = 9.184 Å, b = 5.447 Å and c = 5.145 Å
Density (g cm ⁻³)	4.27	3.90	4.10
Refractive index	2.72	2.52	2.63
Energy band gap (eV)	3.00	3.20	-
Permittivity	114	48	78

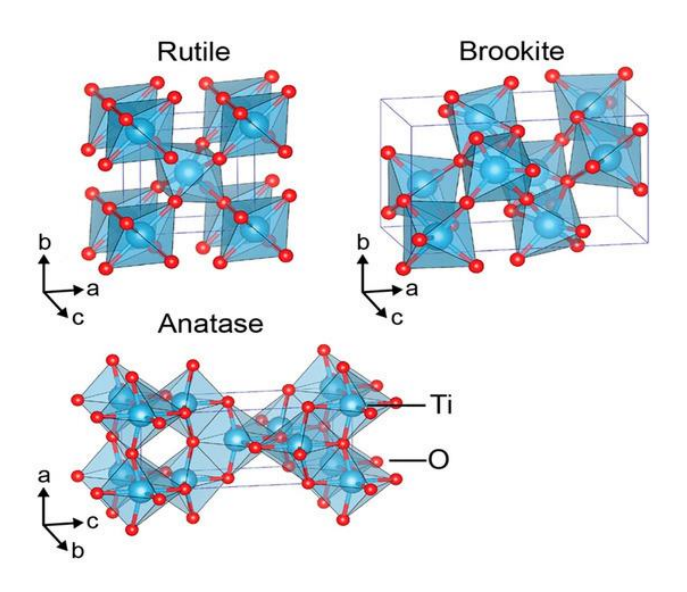


Figure 2.2 Crystal structures of TiO₂ rutile (tetragonal, P42/mmm), brookite (orthorhombic, Pbca), and anatase (tetragonal I41/amd) polymorphs (Haggerty *et al.*, 2017)

Brookite comprises octahedral structures related to the vertical and the edge, whereas rutile comprises octahedral structures connected mainly through their edges. Furthermore, rutile is the most stable phase of TiO₂ minerals, whereas anatase and brookite are metastable TiO₂ phases (Hanaor and Sorrell, 2011). At standard pressure and temperature, the phases of brookite and anatase are almost as stable as rutile due to the slight difference in the free energy that is primarily based on the Gibbs function (Wang *et al.*, 2022, Hanaor and Sorrell, 2011). TiO₂ is typically produced commercially in pyrogenic (chloride process) and precipitation (sulfate process). DuPont company pioneered the chloride process in the late 1950s. By interacting with chlorine gas, the pyrogenic process converted the raw materials of mineral coke into fluid titanium tetrachloride (TiCl₄) (Middlemas *et al.*, 2013). The chloride process starts with combining the raw materials with gaseous chlorine at temperatures ranging between 900-1000°C in a fluidized bed reactor with coke as a reducing agent. The resulting gas stream encompasses titanium tetrachloride (TiCl₄), carbon oxides, and all feedstock impurities in the form of metal chlorides. However,

some impurities, such as silica and zirconium, may not be chlorinated and remain accumulated in the reactor. The following are the main chemical reactions for this process (Braun *et al.*, 1992):

$$2\text{TiO}_2 \text{ (ore)} + 3\text{C} + 4\text{Cl}_2 \rightarrow 2\text{TiCl}_4 \text{ (impure gas)} + 2\text{CO} + \text{CO}_2$$
 (2.1)

$$TiCl_4$$
 (impure gas) \rightarrow $TiCl_4$ (pure liquid) (2.2)

$$TiCl_4 \text{ (pure gas)} + O_2 \text{ (gas)} \rightarrow TiO_2 \text{ (pure solid)} + 2Cl_2$$
 (2.3)

The remaining chlorine from solid TiO₂ is eliminated using aqueous hydrolysis. The pure titanium dioxide is then dried, milled, and subjected to several chemical surface treatments. This process generates rutile crystals with a smaller particle size distribution than sulfate rutile. The sulphate process is a highly exothermic reaction that uses titanium slag, ilmenite, or both in a controlled manner while being digested by concentrated sulfuric acid. It is started by the addition of controlled amounts of steam, water, and diluted sulphuric acid. The digestion reaction equation is given below (raw material dissolution) (McNulty, 2007, Janus, 2017).

$$FeTiO_3 + 2H_2SO_4 \rightarrow TiOSO_4 + FeSO_4 + H_2O$$
 (2.4)

(Dissolution of raw material)

$$TiOSO_4 + H_2O \rightarrow TiO_2 \text{ n.}H_2O + H_2SO_4$$
 (2.5)

(TiO₂ precipitation)

$$TiO_2 \text{ n.H}_2O \rightarrow TiO_2 + nH_2O \tag{2.6}$$

(TiO₂ calcination and conditioning)

After drying, the titanium dioxide is put through a finishing phase that may involve milling or chemical processing, for instance coating the surface with silica or alumina. Similar to the chloride process, the finishing procedure includes milling,

drying, and chemical surface treatments (coating). However, due to the high concentration of iron in ilmenite, the conventional sulphate process yields lower-quality products and large amounts of waste iron sulphate for the majority of applications. Overall, the sulfate process uses a relatively simple technology and lower quality and less expensive raw materials to produce anatase (tetragonal, near octahedral) pigment, which is preferred over chloride pigment for use in papers, ceramics, and inks. Among many applications, TiO₂ is practically the sole material suitable for industrial applications as a photocatalyst in the photocatalytic reaction of organic pollutants.

2.3.2 TiO₂ as Photocatalyst

The most widely used photocatalyst in the photodegradation of water contaminants is TiO₂ due to its high photocatalytic activity, chemical stability, and low biological toxicity. The following are the main reactions for the photocatalytic process (Bagwasi *et al.*, 2013b, Arun *et al.*, 2022).

$$TiO_2 + hv \rightarrow TiO_2 (e_{CB}^- + h_{VB}^+)$$
 (2.7)

$$TiO_2 (h_{VB}^+) + H_2O \rightarrow TiO_2 + H^+ + \bullet OH$$
 (2.8)

$$TiO_2 (h_{VB}^+) + OH^- \rightarrow TiO_2 + \bullet OH$$
 (2.9)

$$TiO_2 (e_{CB}^-) + O_2 \rightarrow TiO_2 + \bullet O_2^-$$
 (2.10)

$$\bullet O_2^- + H^+ \to \bullet HO_2 \tag{2.11}$$

$$\bullet HO_2 + \bullet HO_2 \rightarrow H_2O_2 + O_2 \tag{2.12}$$

$$TiO_2 (e_{CB}^-) + H_2O_2 \rightarrow \bullet OH + OH^-$$
 (2.13)

$$H_2O_2 + \bullet O_2^- \rightarrow \bullet OH + OH^- + O_2$$
 (2.14)

Organic pollutant
$$+ \bullet OH^- \rightarrow degradation product$$
 (2.15)

Organic pollutant +
$$TiO_2 (h_{VB}^+) \rightarrow oxidation product$$
 (2.16)

Organic pollutant +
$$TiO_2$$
 (e_{CB}⁻) \rightarrow reduction product (2.17)

In the process, an electron is excited from the valence band in TiO₂ to the conduction bands when UV light is emitted. The charge carriers of the valence band and the conduction band can recombine and be scavenged. Oxidizing species like OH⁻, H₂O, organic compounds, and reduction species such as O₂ that are present within the solution can also be scavenged by h_{VB}⁺ and e_{CB}⁻, respectively. These combinations primarily lead to the creation of hydroxyl (•OH) radical, hydroperoxyl (•HOO) radical, and superoxide radical anions (•O₂⁻) on the surface of TiO₂, which can destroy a wide range of chemical molecules, including dangerous bio-persistent substances (Humayun *et al.*, 2018, Kumaravel *et al.*, 2019). Figure 2.3 illustrates the technique for degrading organic compounds from textile effluent by UV-TiO₂ (Abdul Mubarak *et al.*, 2022). However, TiO₂ photocatalysts are still inadequate due to their small surface area, irregular particle size, high band gap energy, limited absorption in the visible region, insufficient light absorption, low recycling capacity, secondary pollution development, and rapid recombination of electron-hole pairs, all of which will ultimately lead to lower photodegradation (Bui *et al.*, 2020).

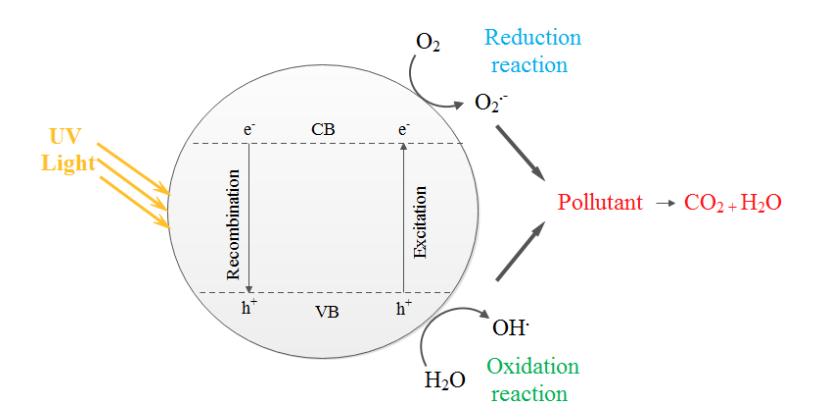


Figure 2.3 The photocatalytic oxidation of organic compounds from textile wastewater under the UV-TiO₂ process

2.3.3 Carbon Porous TiO₂

Carbon porous TiO₂ materials have sparked a lot of interest in photocatalysis because of their outstanding properties. Carbon can enhance the dissociation of electron-hole pairs during TiO₂ photocatalysis due to its superior ability to store electrons. Additionally, it has exceptional qualities such as visible light absorption which aids in the photocatalytic interface reaction (He et al., 2014). The TiO₂ crystal lattice can substitute carbon for either oxygen or titanium, which makes the material a visible light-sensitive photocatalyst (Jhang et al., 2019). Additionally, carbon can precipitate on the surface of TiO₂, acting as a photosensitizer to move the electrons into the conduction band of TiO₂. Apart from that, carbon porous material not only enhances the mass transfer of photocatalytic reactions but encourages the separation of photogenerated electrons and holes and increases quantum efficiency (Crake et al., 2019). The uniform porous structure of TiO₂-based catalysts has attracted a lot of research interest since it can provide a large surface area that significantly boosts the catalytic performance. However, to promote the degradation of organic contaminants, it is crucial to establish easily accessible active sites and prevent agglomeration of the carbonaceous material. A variety of other effective techniques has all been attempted to create carbon TiO2 nanoparticles such as Ti metal pyrolysis, treatment with gaseous carbon sources, and thermal oxidation of titanium carbide (TiC) (Zhang et al., 2013, Kiran and Sampath, 2013). However, as the 21st century approached, attention was drawn to converting metal-organic framework (MOF) into carbonaceous metal oxides as photocatalysts for the photocatalytic treatment of water contaminants due to their tuneable structures and high porosity.

2.4 Metal-Organic Frameworks

Over the past decade, metal-organic frameworks (MOFs) have extensively been explored and emerged on the lab and industrial scale. MOF is a molecular network that contains both organic and inorganic bonding. It is constructed by metal clusters or ions (also known as secondary building units) and organic linkers (Batten et al., 2013). Multidentate organic molecules, for example, halides, cyanides, neutral organic molecules, and anionic organic molecules, are typically the organic linkers used to connect the metal nodes in coordination polymers (Nasalevich et al., 2014, Alhamami et al., 2014). The aromatic rings of the framework's linkers control the structure's geometry and help preserve the complex's structural integrity. These properties are mainly due to the hydrophobic nature and rigid structure of the aromatic rings. Metal clusters are considered the inorganic secondary building units (SBUs), which act as joints in MOF (Yaghi et al., 2003). SBUs geometries can be square-planar, linear, tetrahedral, octahedral, square-pyramidal, trigonal prismatic, or trigonal bipyramidal, according to the metal coordination numbers involved in the center (Evans et al., 2019). Combining these two organic and inorganic matters through synthesis can achieve various characteristics, for example, high porosity, large surface area, and low density (Zhou et al., 2012). It is possible to organize the pore volume and surface area of MOF by changing organic ligands that serve as spacers and create open porous structures (Sun et al., 2017). These porous structures have sizes ranging from micro to meso with substantially high surface energy (Butova et al., 2016). High interior surface areas linked to porosity enhance the adsorption of guest molecules.

Additionally, the MOF structures can be easily tuned by changing the metal nodes or ligands that enable a custom-made MOF with suitable design and

functionalities needed for particular applications (Vlasova *et al.*, 2016). Due to these attractive features, widespread applications have been explored mainly in gas storage and separation, heterogeneous catalysis, chemical sensing, and biomedical (Cheong and Moh, 2018). Thousands of articles appeared when searching for the keyword of MOF or metal-organic frameworks. The most typical MOFs studied are Hong Kong University of Science and Technology (HKUST-1), Material of Institute Lavoisier (MIL-101), Zeolitic Imidazolate Framework (ZIF-8), and Universitetet i Oslo (UiO-66). MOFs demonstrate extraordinarily high stability, simple synthesis methods, and great suitability for a variety of applications, especially gas storage. Apart from that, their structural and practical application has caused a growing interest in these materials in chemistry and other related fields.

The design of the MOF structure is based on the construction of any metallic compound under controlled conditions. For the past decade, many studies have been devoted to synthesizing MOF using di-, tri-, or tetravalent metal ions. Divalent metal ions, notably Cu²⁺, Zn²⁺, Co²⁺, and Ni²⁺ (MOF-5, MOF-74, HKUST-1, etc.), have been reported to show a weak interaction between the metal ions with the organic ligands, mainly due to their poor water stability, that will eventually restrict their widespread application (Shi *et al.*, 2019). On the other hand, trivalent and tetravalent metal ions, such as Fe³⁺, Al³⁺, Cr³⁺, Ti⁴⁺, Zr⁴⁺, and Hf⁴⁺, have better stability due to their high valence cations (Horcajada *et al.*, 2007, Lebedev *et al.*, 2005). Consequently, MOF with tetravalent metal cations has attracted high interest, enabling their use in extensive practical applications. Compared to MOF developed from other metals, two key components explaining why tetravalent metals cations have substantially improved chemical stability and are vastly preferable: 1) these cations exhibit a higher charge and charge-to-radius ratio (Z/R), making them hard

acids that better associate with the hard carboxylate oxygens found in most MOF ligands and thus produce stronger ionic interactions, and 2) the MOF structures formed have significantly more nuclearity than other MOF SBUs (Stock and Biswas, 2012). According to the requirements of the MOF's topology, SBUs may have various but high connectivity with 12, 8, or 6 connected SBUs (Kalmutzki *et al.*, 2018). Therefore, titanium is regarded as a highly desirable candidate for constructing MOFs.

2.5 Ti-based MOF

Titanium (Ti)-based MOFs are the most interesting MOFs due to the tetravalent cation that shows excellent redox activity and robust metal-ligand bonding with a rigid framework (Ockwig *et al.*, 2005, Yang *et al.*, 2019a). In ambient conditions, the +4-oxidation state is the most stable. Rapid and spontaneous hydrolysis takes place in a very acidic medium as a result of the reduced electronegativity of Ti and the increased polarising power of Ti⁴⁺, which causes uncontrolled precipitation of TiO₂. The critical factors for stabilizing the Ti (+4) ion in the solution are the titanium precursor, the strength of the organic ligand, and the pH of the media. The two most commonly used precursors are titanium chloride and titanium alkoxides. However, titanium chloride is not commonly preferred because it produces hydrochloric acid and is susceptible to hydrolysis. As a result, titanium alkoxides are preferable due to the hydrophobic nature of the alkoxy groups and their ability to hinder steric interactions (Assi *et al.*, 2017).

In addition, organic linkers such as carboxylates, phosphonates, catecholate, and salicylates are well-suited to pair with Ti (+4) cations because of their bidentate properties. This results in a higher coordination number that enhances their stability

in water (Ahmed and Jhung, 2017). Additionally, Ti appeared to be the most engaging material for creating the MOF framework due to its high chemical stability and diverse functional structure. The unique attributes of Ti-based MOFs, including their affordability, non-toxicity, versatility, biocompatibility, and favorable redox activity (transition between Ti³⁺ to Ti⁴⁺), make them an intriguing material (Smolders *et al.*, 2019). For example, MIL-125(Ti) is built from Ti(+4) with 12-connected SBUs, and the high connectivity of the clusters makes this MOF more resilient to the replacement of ligands with alternative nucleophiles such as water (Shi *et al.*, 2019).

2.6 MIL-125(Ti)

Pristine MIL-125(Ti) or Ti₈O₈(OH)₄–(O₂C–C₆H₄–CO₂)₆ has an orthorhombic face-centered cubic (**fcu**) topology built by Ti₈O₈(OH)₄ clusters and 1,4-benzenedicarboxylate linkers Figure 2.4. MIL-125(Ti) is constructed from cyclic octamers built from corner or edge-sharing and composed of eight TiO₆ octahedral titanium units connected to oxygen atoms (Yan *et al.*, 2020). The structure is a cubic arrangement of ring-shaped body-centered Ti₈O₈(OH)₄(-COO)₁₂ SBUs.

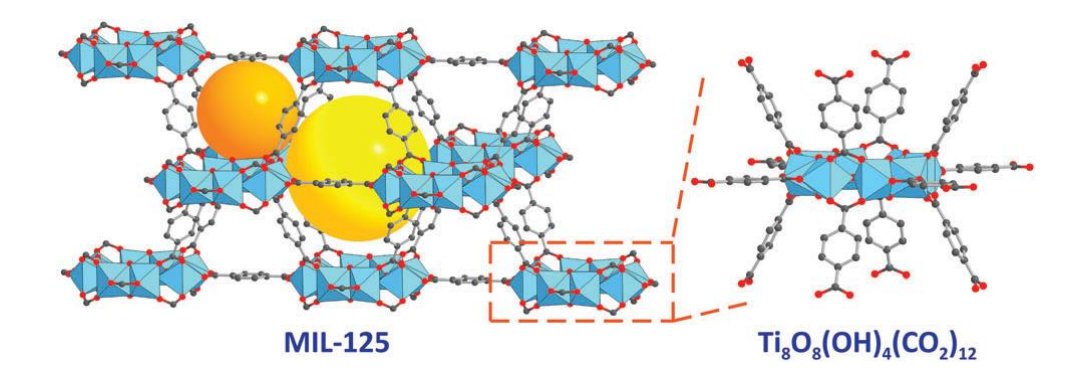


Figure 2.4 Crystal structure of MIL-125(Ti). The structure can be described as a body-centered arrangement of ring-shaped Ti₈O₈(OH)₄(–COO)₁₂ SBUs connected by linear diatopic BDC linkers. The resulting augmented **bcu** net has two distinct pores corresponding to the tetrahedral and octahedral holes of a body-centered cubic packing. All hydrogen atoms are omitted for clarity. Color code: Ti, blue; C, gray; O, red (Nguyen, 2017)